Seismological evidence for grain-size sensitive olivine deformation during mid-ocean ridge spreading

Joshua B. Russell,[1*] James B. Gaherty,[2,3] Hannah F. Mark,[4] Greg Hirth,[1]
Lars N. Hansen,[5] Daniel Lizarralde,[6] John A. Collins,[6] Rob L. Evans[6]

[1]Department of Earth, Environmental and Planetary Sciences, Brown University, Providence, RI, USA

[2]Lamont-Doherty Earth Observatory of Columbia University, Palisades, NY, USA

[3]School of Earth and Sustainability, Northern Arizona University, Flagstaff, AZ, USA

[4]Department of Earth and Planetary Sciences, Washington University in St. Louis, St. Louis, MO, USA

[5]Department of Earth and Environmental Sciences, University of Minnesota, Minneapolis, MN, USA

[6]Woods Hole Oceanographic Institution, Woods Hole, MA, USA

[*]To whom correspondence should be addressed; E-mail: joshua_russell@brown.edu.

Key Points:

- The first *in situ* elastic tensor for shallow oceanic lithosphere is estimated, incorporating compressional and shear anisotropy constraints
- Comparing anisotropy to laboratory samples indicates that shear strain of 300–400% was accumulated during mid-ocean ridge spreading
- D-type olivine fabric implies near-ridge deformation dominated by grain-size sensitive dislocation-accommodated grain boundary sliding

Abstract

Seismic anisotropy produced by aligned olivine in oceanic lithosphere offers a window into mid-ocean ridge dynamics and the state of Earth's upper mantle. Yet, interpreting anisotropy in the context of grain-scale deformation processes observed in laboratory and natural olivine samples has proven challenging due to the vast length scale differences. We bridge this observational gap by estimating the first *in situ* elastic tensor of oceanic lithosphere using compressional- and shear-wavespeed anisotropy observations, with fast azimuth parallel to the fossil-spreading direction. This observation is compared with a database of 123 petrofabrics from the literature to infer olivine crystallographic orientations and shear strain accumulated within the lithosphere. Findings indicate D-type olivine lattice-preferred orientation (LPO) with girdled [010] and [001] crystallographic axes and strain accumulation of 300–400%, challenging the prevailing assumption of A-type LPO. This LPO is consistent with olivine deformation during seafloor spreading via grain-size sensitive dislocation-accommodated grain boundary sliding (disGBS), rather than grain-size insensitive dislocation creep. Such deformation implies *in situ* grain sizes of 0.3–15 mm, smaller on average than steady-state predictions for pure olivine from laboratory calibrations, which may be attributed to grain-boundary pinning by secondary phases or an underestimate of the importance of disGBS by standard flow laws. This work demonstrates the ability to integrate laboratory- with seismological-scale observations of seismic anisotropy and provides new constraints on *in situ* grain size and associated rheology during near-ridge mantle deformation.

Plain Language Summary

Earth's upper mantle is composed primarily of the mineral olivine, which responds to shear deformation by organizing with its seismically fast axis parallel to the deformation direction. During mid-ocean ridge spreading, olivine crystals that align parallel to spreading freeze into the lithosphere preserving the near-ridge deformation history. The resulting rock fabric is observed in place via the directional dependence of seismic waves (seismic anisotropy) as well as in hand-sample rocks collected from the field. However, interpreting *in situ* observations of seismic anisotropy in the context of laboratory and field data remains a challenge, due to large differences in length scale and incomplete seismic constraints. Here, we bridge this observational gap by solving for the complete anisotropic structure of ∼70 Ma oceanic lithosphere by incorporating multiple data types. Our model is compared to laboratory data in order to infer the magnitude of shear strain and style of olivine deformation during mid-ocean ridge spreading. Our results indicate large shear strains of 300–400% and an alternative olivine fabric style

to that typically assumed, implying deformation by sliding along individual grain boundaries in addition to dislocation within grains. This has new implications for the formation and evolution of oceanic plates and mid-ocean ridge dynamics.

1 Introduction

Observations of seismic anisotropy in the ocean basins provide unparalleled insight into Earth's mantle circulation patterns, including the plate-tectonic process of seafloor spreading (*Forsyth*, 1975, *Gaherty et al.*, 2004, *Hess*, 1964, *Lin et al.*, 2016, *Mark et al.*, 2019, *Montagner and Tanimoto*, 1991, *Nishimura and Forsyth*, 1989, *Takeo et al.*, 2018, *Toomey et al.*, 2007). Based on olivine lattice-preferred orientation (LPO) observed in peridotites sampled from ophiolites and oceanic settings (*Ben-Ismail and Mainprice*, 1998, *Michibayashi et al.*, 2006, *Peselnick and Nicolas*, 1978, *Skemer et al.*, 2010, *Warren et al.*, 2008) and in deformation experiments on olivine (*Bystricky et al.*, 2000, *Zhang and Karato*, 1995, *Zhang et al.*, 2000), upper-mantle anisotropy has historically been interpreted as evidence that deformation associated with mantle convection and plate tectonics occurs via dislocation creep in an olivine-rich upper mantle (*Karato and Wu*, 1993). This inference in turn constrains key physical parameters such as grain size, and more generally, the rheology of the upper mantle (*Hirth and Kohlstedt*, 2003).

Subsequent advances in laboratory deformation experiments on olivine have complicated this interpretation, however, illuminating several olivine slip systems and associated LPO fabric types that may depend on mantle conditions such as stress, volatile content, and partial melting (*Bystricky et al.*, 2000, *Jung and Karato*, 2001, *Jung et al.*, 2006, *Katayama et al.*, 2004, *Qi et al.*, 2018). The three most commonly observed types of olivine LPO in experiments and natural settings are A-, E-, and D-type, each with their fast [100] crystallographic axis oriented sub-parallel to the shear direction but with variable orientations of the slow [010] and intermediate [001] axes (Figure 1). Due to incomplete *in situ* shear and compressional constraints, it has not been possible to distinguish between these three fabric types in oceanic lithosphere using traditional seismological observations, leading to renewed ambiguity on physical state and deformation processes during seafloor spreading (*Karato et al.*, 2008).

Here, we combine a unique high-resolution estimate of seismic anisotropy in Pacific lithosphere with a database of 123 olivine petrofabrics reported in the literature from experimentally and naturally deformed rocks to directly constrain olivine LPO type and associated deformation mechanism and to quantify

shear strain associated with seafloor spreading. The new seismic model, NoMelt_SPani, combines a co-located set of compressional and shear anisotropy observations in the central Pacific (*Mark et al.*, 2019, *Russell et al.*, 2019), resulting in an exceptionally complete estimate of peridotite elasticity in the oceanic lithosphere. The collection of laboratory and field petrofabric observations provide a framework for quantitative interpretation of the *in situ* elasticity tensor in terms of degree of strain, composition, LPO type, and deformation mechanism.

2 Data

2.1 Seismic observations at the NoMelt experiment

The NoMelt geophysical experiment in the central Pacific provided unique co-located compressional- and shear-wave constraints (V_{P} and V_{S}, respectively) on *in situ* lithosphere petrofabric over a 600×400 km footprint with average seafloor age of ∼70 Ma. It comprised a refraction survey that constrained V_{PH} and its azimuthal anisotropy in the upper ∼7 km of the mantle (*Mark et al.*, 2019) and a broadband OBS deployment that resolved the complete V_{S} structure via observations of both Rayleigh-wave (*Lin et al.*, 2016) and Love-wave azimuthal anisotropy (*Russell et al.*, 2019) in the upper 40 km of the lithosphere. Together, these independent compressional and shear observations of seismic anisotropy probe the complete elastic tensor of oceanic lithosphere.

2.2 Olivine fabric database

We have compiled a database of the elastic properties of 123 published olivine fabrics that includes 91 olivine samples deformed in the laboratory by direct shear (*Jung and Karato*, 2001, *Jung et al.*, 2006, *Katayama et al.*, 2004, *Zhang and Karato*, 1995) and high-strain torsion (*Bystricky et al.*, 2000, *Hansen et al.*, 2014, 2016) experiments, as well as 31 natural peridotite samples from diverse settings including ophiolites (*Ben-Ismail and Mainprice*, 1998, *Michibayashi et al.*, 2006, *Peselnick and Nicolas*, 1978, *Skemer et al.*, 2010, *Warren et al.*, 2008), volcanic arcs (*Mehl et al.*, 2003), and xenoliths and kimberlites from continental cratons (*Ben-Ismail et al.*, 2001, *Satsukawa et al.*, 2010). Of these samples, 42 (31 natural and 11 laboratory) have had LPO identified by the authors based on the orientations of their crystallographic axes: 12 have been identified as A-type, 6 E-type, and 24 D-type. The methods employed by previous authors to calculate bulk seismic properties from individual crystallographic orientations

generally follow a similar procedure and (1) nearly ubiquitously assume samples are composed of 100% olivine and (2) use the single-crystal olivine tensor of *Abramson et al.* (1997). For one harzburgite sample from the Oman ophiolite, the seismic properties were measured directly using ultrasonics, and therefore, contributions from other phases are inherently included (*Peselnick and Nicolas*, 1978). The temperature and pressure conditions at which the elastic calculations are carried out can vary slightly among studies but has negligible effect on seismic anisotropy (*Ben-Ismail and Mainprice*, 1998).

For all samples considered, the orientation of the elastic tensor with respect to the shear plane and shear direction were determined. Upon comparing to the seismic model, all samples in the database were oriented in the seismic reference frame: shear plane parallel to the X-Y plane defined by Earth's surface and shear direction parallel to the X-axis defined by the fossil-spreading direction (FSD). The Z-axis is oriented perpendicular to Earth's surface (i.e., perpendicular to the shear plane).

Estimates of shear strain associated with deformation are routinely measured for laboratory samples and range from undeformed ($\gamma \sim 0$) to $\gamma \sim 18.7$ in our dataset, but such estimates are rarely available for natural rocks. One exception is the Josephine shear zone in southwestern Oregon (*Hansen and Warren*, 2015, *Warren et al.*, 2008), which has pre-existing foliations that provide passive strain markers that imply highly strained peridotites up to $\gamma \sim 20$ (*Skemer et al.*, 2010).

3 Methods

3.1 Surface-wave inversion with $P_{\mathbf{n}}$ constraints

We invert previously measured Rayleigh- and Love-wave phase velocity for the shear and compressional velocities and anisotropy beneath the NoMelt array to 400 km depth as in *Russell et al.* (2019) but only focus here on the upper ∼7 km of the mantle, for which both P and S constraints exist. Previously measured anisotropic Rayleigh- (5–150 s) and Love-wave (5–7.5 s) phase velocities from *Russell et al.* (2019) are inverted, while simultaneously satisfying V_{P} constraints in the upper ∼7 km of the mantle from *Mark et al.* (2019) ("Weighted data, with gradients" in their Table 1). The inversion is carried out in two steps following *Russell et al.* (2019): (1) Rayleigh and Love phase velocity dispersion are inverted for seismic velocities $V_{\mathrm{SV}} = \sqrt{L/\rho}$, $V_{\mathrm{SH}} = \sqrt{N/\rho}$, $V_{\mathrm{PV}} = \sqrt{C/\rho}$, and $V_{\mathrm{PH}} = \sqrt{A/\rho}$ with $\eta = F/(A-2L)$ fixed to PREM values (*Dziewonski and Anderson*, 1981) and V_{PH} in the upper 7 km of the mantle fixed to values from *Mark et al.* (2019). V_{PV} is scaled such that $\phi^{-1} = (V_{\mathrm{PH}}/V_{\mathrm{PV}})^2$ remains equal to

$\xi = (V_{\mathrm{SH}}/V_{\mathrm{SV}})^2$. (2) The observed magnitude of azimuthal anisotropy and fast direction of Rayleigh and Love waves are inverted to determine the depth-dependent magnitude and direction of azimuthal anisotropy elastic parameters G/L, B/A, H/F, and E/N (see *Russell et al.* (2019) Appendix). The 2θ and 4θ dependence of P_{n} provides independent constraints on the magnitude and azimuth of B and E, respectively via

$$\rho V_{P\mathrm{n}}(\theta)^2 = A + B_{\mathrm{c}}\cos(2\theta) + B_{\mathrm{s}}\sin(2\theta) + E_{\mathrm{c}}\cos(4\theta) + E_{\mathrm{s}}\sin(4\theta) \tag{1}$$

and enters the surface-wave inversion simply as prior constraints on B and E. Below ∼7 km beneath the Moho, at which P_{n} constraints terminate, and for the parameter H, we follow the general scaling approach described in *Russell et al.* (2019), whereby B and H scale directly with G. For this study, the direct B and G constraints in the upper 7 km suggest an empirical B/G scaling of ∼1.5 that is applied throughout the model. Additionally, an H/G scaling of -0.11 is applied based on ophiolite samples (*Ben-Ismail and Mainprice*, 1998, *Peselnick and Nicolas*, 1978).

3.2 Constructing the orthorhombic elastic tensor

A general elastic tensor is described by 21 independent elastic parameters. This tensor is simplified to only 9 parameters (A, C, F, L, N, G, B, H, E) if orthorhombic symmetry is assumed and the three orthogonal crystallographic axes ([100], [010], [001]) are oriented along the principal directions (i.e., in the principal coordinate system). In this configuration, any crystallographic axis may be oriented along any of the three principal directions. This requirement is relaxed for the two horizontal directions in order to allow for arbitrary orientations of azimuthal anisotropy in the horizontal plane, resulting in an elastic tensor with 13 parameters (*Montagner and Nataf*, 1986). As one axis is assumed to be vertical (a requirement given that surface waves are horizontally propagating), dipping fabrics are not explicitly

resolvable. The symmetric elastic tensor is given by

$$C_{ij} = \begin{pmatrix} A + B_{\mathrm{c}} + E_{\mathrm{c}} & A - 2N - E_{\mathrm{c}} & F + H_{\mathrm{c}} & 0 & 0 & \frac{1}{2}B_{\mathrm{s}} + E_{\mathrm{s}} \\ \cdot & A - B_{\mathrm{c}} + E_{\mathrm{c}} & F - H_{\mathrm{c}} & 0 & 0 & \frac{1}{2}B_{\mathrm{s}} - E_{\mathrm{s}} \\ \cdot & \cdot & C & 0 & 0 & H_{\mathrm{s}} \\ \cdot & \cdot & \cdot & L - G_{\mathrm{c}} & G_{\mathrm{s}} & 0 \\ \cdot & \cdot & \cdot & \cdot & L + G_{\mathrm{c}} & 0 \\ \cdot & \cdot & \cdot & \cdot & \cdot & N - E_{\mathrm{c}} \end{pmatrix}. \quad (2)$$

Although we solve for all 13 parameters of the tensor in the upper 7 km of the mantle, only 9 are independently determined by our observations (L, N, A, $G_{\mathrm{c,s}}$, $B_{\mathrm{c,s}}$, $E_{\mathrm{c,s}}$). The remaining four terms that require scaling assumptions (C, F, $H_{\mathrm{c,s}}$) do not contribute to the quantitative comparisons between the *in situ* tensor and the natural and laboratory petrofabrics.

3.3 Accounting for pyroxene in anisotropy calculations

Secondary phases in addition to olivine in a given sample act to reduce the bulk strength of seismic anisotropy (*Bernard et al.*, 2021), yet most values reported for laboratory and natural petrofabrics only consider aggregates of pure olivine. In order to directly compare these samples against our *in situ* estimate, which inherently includes bulk chemistry, we approximate the influence of secondary phases on seismic anisotropy following *Hansen et al.* (2014). Mineral physics calculations using the tool Perple_X (*Connolly*, 2009) suggest the shallow lithospheric mantle is comprised of ∼60 vol.% olivine assuming an upper mantle composition consistent with standard depleted mid-ocean ridge basalt (MORB) mantle composition (*Hacker*, 2008) and a half-space cooling temperature profile for 70 Ma (Figure S1). Invoking the simplifying assumption that the remaining 40% by volume can be approximated by orthopyroxene, a composite elastic tensor is constructed for each sample by taking the Voigt average between the olivine tensor and an orthopyroxene texture from *Hansen et al.* (2014) (Figure S2). This assumption acts to

reduce the overall strength of the fabric without having a large effect on the fast propagation azimuth (*Bernard et al.*, 2021).

For samples in which reported anisotropy strengths were used instead of calculated from an elastic tensor, an empirical scaling was applied to account for the effect of pyroxene. Considering only well-developed fabrics with $\gamma > 2$ from the laboratory data of *Hansen et al.* (2014, 2016), fabric strength was calculated with orthopyroxene content ranging from 0% to 100% by volume for each sample and was fit with a linear function (Figure S3). The relationship between pyroxene content and reduction of anisotropy magnitude is nearly -1:1 and provides a straightforward method for scaling anisotropy magnitude.

4 Results

4.1 A comprehensive elastic model of oceanic lithosphere

Previously measured high-frequency ambient-noise Rayleigh- and Love-wave phase velocities were inverted incorporating co-located P_n constraints for the complete elastic structure at NoMelt. The resulting model, NoMelt_SPani, is shown in Figure 2, and here we focus on the upper ∼7 km beneath the Moho for which P- and S-constraints coincide. Azimuthal anisotropy increases with depth beneath the Moho for both G (V_{SV}) and B (V_{PH}), but remains relatively constant for E (V_{SH}), largely due to the lack of Love-wave depth sensitivity (*Russell et al.*, 2019). Anisotropy fast azimuths Ψ_G and Ψ_B are sub-parallel to the fossil-spreading direction (FSD), and Ψ_E is rotated by 45°, as predicted for orthorhombic olivine (*Montagner and Nataf*, 1986). In detail, while Ψ_G and Ψ_B are each consistent with FSD within error, they differ from one another by 5–10°. This subtle mismatch is likely attributed to the different depth sensitivities of P_n and surface waves: the refraction imaging is primarily sensitive to the shallowest ∼7 km of the mantle, while the surface waves integrate across the upper ∼20 km.

From the 13 elastic parameters, we construct the equivalent orthorhombic elastic tensor at each depth and average the upper 7 km to produce a single representative elastic tensor, NoMelt_SPani7, given in Table 1. The tensor has been rotated into the seismic reference frame such that X is parallel to the FSD, Y is perpendicular to the FSD and parallel to Earth's surface, and Z is perpendicular to Earth's surface. The V_P pole figure shown in Figure 2c indirectly expresses the relative orientations of the three crystallographic axes. The well-defined maximum parallel to the FSD indicates a sub-horizontal, clustered [100] fast axis. The girdled slow and intermediate directions indicate dispersed [010] and [001]

axes perpendicular to the inferred shear direction, characteristic of D-type olivine fabric (Figure 1b).

4.2 Strain accumulation in the shallow lithosphere

Olivine LPO strength, and in turn the magnitude of seismic anisotropy, increases with shear strain (*Hansen et al.*, 2014, 2016). The NoMelt model provides four independent estimates of the magnitude of seismic anisotropy and three independent estimates of anisotropic directions that can be directly compared to olivine LPO formed as a function of strain (Figure 3). We compare NoMelt_SPani7 to samples deformed in laboratory torsion experiments (*Hansen et al.*, 2014, 2016) as well as to samples deformed naturally in a shear zone in the Josephine Peridotite (*Hansen and Warren*, 2015, *Warren et al.*, 2008), for which strain has been determined.

When 100% olivine is assumed, the high strains required to match the orientation of fast directions in Figure 3f–h correspond to magnitudes of anisotropy in Figure 3a–d that are approximately twice that which we observe. As the NoMelt model represents harzburgitic oceanic lithosphere, it is not surprising that a direct comparison to pure olivine fabrics fails to find a range of shear strains compatible with the seismic model. Incorporating the effect of composition on the sample fabrics by accounting for the presence of pyroxene helps resolve this discrepancy. For each sample, we approximate the contributions from pyroxene by combining each pure olivine elastic tensor with the tensor for an appropriately oriented orthopyroxene texture following *Hansen et al.* (2014) as described in Section 3.3. We assume a nominal harzburgite composition of 60% olivine and 40% orthopyroxene by volume, which represents the lower bound of olivine content in abyssal peridotites observed globally (*Warren*, 2016). For the natural samples from *Hansen and Warren* (2015), dunite samples are used for the 100% olivine case, while harzburgite samples with 40% orthopyroxene added are used for the 60% olivine case. This composition is also consistent with the average lithospheric V_P and V_S in the NoMelt model, as compared to Perple_X calculations (*Connolly*, 2009) for a typical depleted mid-ocean ridge basalt (Figure S1). Compared to the pure olivine estimates, the mixture systematically decreases the strength of anisotropy due to orthopyroxene's weaker single-crystal anisotropy and LPO compared to olivine, while fast azimuths are largely unaffected, consistent with the recent findings of *Bernard et al.* (2021), who investigate a large suite of upper mantle xenoliths.

The overall agreement between NoMelt anisotropy and the laboratory torsion data for 60% olivine is remarkable given the vast difference in length scale of the measurements (∼9 orders of magnitude

assuming a seismic wavelength on the order of ∼100 km and laboratory LPO texture measurements of ∼100 μm). The magnitude of anisotropy at NoMelt is consistent with laboratory samples for shear strains ranging from 2 to 4, and the orientation of fast directions is consistent with $\gamma > 3$. We therefore infer that this portion of the upper mantle was subject to shear strains ranging from 3 to 4, which is on the upper end of that expected at shallow depths during seafloor spreading (*Tommasi*, 1998). The angle between the fast V_P axis and inferred shear plane is small ($\lesssim 10°$) for $\gamma > 1.5$ (Figure 3e), implying a sub-horizontal concentration of [100] crystallographic axes, in agreement with previous work (*Skemer et al.*, 2012). This observation suggests a horizontal fabric at NoMelt, though we are unable to directly constrain fabric dip with our dataset that consists only of horizontally propagating waves.

The strain evolution of natural samples is more scattered and exhibits clear differences from the experimental samples. For a given strain and olivine content, the magnitude of anisotropy of the natural fabrics is consistently weaker. This is perhaps unsurprising given the differences in scale between natural shear zones, such as at the Josephine ophiolite, and laboratory torsion experiments. In addition, the anisotropy fast directions of the natural samples fail to consistently rotate into the shear direction with increasing strain, remaining misaligned by ∼25° at $\gamma = 5.25$ (Figure 3f–h). The relatively weak and misaligned anisotropy of the highly strained Josephine samples is likely attributed to the presence of a pre-existing LPO prior to shear zone development, which prolongs fabric development and misalignment of [100] with respect to the shear direction (*Skemer et al.*, 2012, *Warren et al.*, 2008). Uncertainties associated with measuring orientations in the field and preparing oriented samples for electron backscatter diffraction (EBSD) measurements in the lab may also contribute to scatter. That NoMelt anisotropy is stronger than even the most highly strained natural sample ($\gamma = 5.25$) with 60% olivine, highlights the remarkably coherent LPO in the lithosphere across the 600×400 km NoMelt footprint (*Russell et al.*, 2019). In addition, it suggests that any pre-existing vertical LPO associated with upwelling at the ridge was likely weak in comparison to that imposed after corner flow and therefore overprinted.

Strain evolution of LPO from D-type at intermediate strains to A-type at high strains was previously identified by *Hansen et al.* (2014). This LPO evolution is reflected in the average V_P surfaces shown above Figure 3a. The inferred shear strain at NoMelt of 3–4 based on strength and direction of anisotropy in comparison to laboratory samples corresponds to fabrics with girdled slow and intermediate V_P directions on average, consistent with D-type LPO.

4.3 Inferring LPO fabric type

We further investigate LPO fabric type by comparing the relative magnitudes of azimuthal and radial anisotropy, which provides a discriminant of LPO type if the orientation of the sample with respect to the shear plane is known (*Karato*, 2008, *Karato et al.*, 2008) (Figure 1). The idea is similar to the more general Flinn diagram method of *Michibayashi et al.* (2016) based on ratios of V_P along different crystallographic directions and was recently proposed as a way to distinguish intrinsic LPO from extrinsic anisotropy mechanisms such as compositional layering or oriented melt pockets (*Hansen et al.*, 2021). In Figure 4, we compare the strength of NoMelt anisotropy with that calculated for A-, D-, and E-type olivine fabrics from both natural settings (*Ben-Ismail and Mainprice*, 1998, *Ben-Ismail et al.*, 2001, *Karato*, 2008, *Mehl et al.*, 2003, *Michibayashi et al.*, 2006, *Peselnick and Nicolas*, 1978, *Satsukawa et al.*, 2010, *Skemer et al.*, 2010, *Warren et al.*, 2008) and laboratory deformation experiments (*Bystricky et al.*, 2000, *Jung and Karato*, 2001, *Jung et al.*, 2006, *Katayama et al.*, 2004, *Zhang et al.*, 2000). For most samples, the LPO type was characterized by the original authors.

To first order, samples with A-type LPO tend to exhibit strong radial anisotropy relative to azimuthal, whereas the opposite is true for E-type. NoMelt displays moderate radial and azimuthal anisotropy most similar to the samples with D-type LPO. This result holds regardless of the olivine content assumed (Figure S4), though we find that a composition of 75% olivine and 25% orthopyroxene provides the best overall fit to the seismic observations. As the D-type LPO data in Figure 4 represent mostly natural samples, the higher olivine content required to match the seismic model is consistent with Figure 3, which showed that natural samples underestimate the magnitude of anisotropy for 60% olivine and 40% orthopyroxene. The true pyroxene content of the Josephine harzburgites ranges 12.8–35.1% (*Hansen and Warren*, 2015), and accounting for this fact would bring the natural samples closer to the NoMelt observations of B/A, G/L, and E/N in Figure 3. A harzburgite composition with 75% olivine is also consistent with abyssal peridotites from fast-spreading MORs, which tend to have higher olivine content (70–95%) compared to slow-spreading MORs (*Dick and Natland*, 1996, *Niu and Hékinian*, 1997, *Warren*, 2016). If lower pyroxene content is assumed, the relationship in Figure 3a–d would indicate a moderately lower magnitude of strain at NoMelt that is inconsistent with the higher strains implied by the anisotropy fast orientations parallel to the shear direction Figure 3f–h.

Scatter among samples of the same fabric type in Figure 4 is likely attributed to differences in shear strain, with low strain samples exhibiting weaker anisotropy, as demonstrated in Figure 3a–d. At lower

shear strains (and in the presence of a pre-existing LPO) dip of [100] with respect to the shear plane is common (*Skemer et al.*, 2012) (Figure 3e), resulting in weaker radial and azimuthal anisotropy. Therefore, dipping fabrics in Figure 4 will tend to skew towards the origin, which does not change the overall inference of D-type LPO (Figure S5). In other cases, scatter may be attributed to samples that straddle the boundary between two LPO types, such as the peridotite averages of *Ben-Ismail and Mainprice* (1998), which are composed of both A-type and D-type samples.

5 Discussion

5.1 D-type LPO and implications for creep mechanism

The relative strengths of radial and azimuthal anisotropy (Figure 4), as well as the range of inferred strain (Figure 3a) are consistent with D-type LPO at NoMelt. Although A-type LPO is typically considered most prevalent in the upper mantle, D-type is also commonly observed in nature; yet, the conditions under which they form are still debated. D-type LPO has been produced in laboratory experiments on fine-grained olivine aggregates deformed under dry, high-stress conditions (*Bystricky et al.*, 2000, *Carter and Ave'Lallemant*, 1970, *Jung et al.*, 2006), but such stresses are unlikely to be present during ridge corner flow or in the asthenosphere.

Girdled D-type LPO has been modeled by relaxing the von Mises strain compatibility criteria (*Tommasi et al.*, 2000), possibly facilitated by grain-boundary sliding processes (*Warren et al.*, 2008). There is increasing evidence that D-type LPO forms under a range of natural conditions through grain-size sensitive dislocation-accommodated grain boundary sliding (disGBS). In ophiolites, A- and D-type LPO have been observed in course-grained dunites and finer-grained harzburgites, respectively, suggesting pyroxene may play a role in D-type LPO formation by limiting olivine grain size and promoting deformation by disGBS (*Braun*, 2004, *Warren et al.*, 2008). Indeed, contributions from pyroxene are important for reconciling the NoMelt observation with laboratory data. Recalibrated olivine flow laws suggest that disGBS may be active at a range of stresses and grain sizes that are appropriate for upper-mantle deformation (*Hansen et al.*, 2011). MOR geodynamic modeling that incorporates grain-size evolution and mixed deformation processes (diffusion creep, dislocation creep, and disGBS) suggest that shallow, near-ridge deformation is dominated by disGBS (*Turner et al.*, 2015).

5.2 *In situ* grain size and stress

We interpret D-type LPO in the upper ∼7 km of mantle as observational evidence for deformation dominated by grain-size sensitive disGBS, rather than grain-size insensitive dislocation creep. The implications for *in situ* grain size are evaluated using olivine flow laws. A deformation mechanism map is presented in Figure 5a for reasonable sub-Moho conditions at the MOR ($T = 1250°C$, $P = 360$ MPa) and olivine flow law parameters from *Hansen et al.* (2011) (Table S3). Assuming tectonic strain rates of $10^{-14.5}$–$10^{-12.5}$ s^{-1} for disGBS implies *in situ* grain sizes of 0.3–15 mm and relatively low stress (0.2–1.4 MPa), broadly consistent with recent geodynamic modeling (*Turner et al.*, 2015, 2017). These inferred low stresses are at odds with the notion that D-type LPO forms only at high stress (*Jung et al.*, 2006, *Karato et al.*, 2008), an idea resulting from laboratory experiments at small grain sizes deformed under high strain rates unrepresentative of mantle conditions.

The grain sizes inferred from conditions where disGBS is predicted to be the dominant deformation mechanism (Figure 5a) are slightly smaller on average than the steady-state predictions of ∼5–50 mm from the laboratory-calibrated grain-size piezometer (*Hirth and Kohlstedt*, 2015, *Karato et al.*, 1980) and wattmeter (*Austin and Evans*, 2007) (see Appendix A for details of wattmeter calculation). However, by considering the uncertainty in the flow law parameters (see Appendix B for details), scenarios in which the disGBS field expands to larger grain sizes coinciding with the piezometer and wattmeter predictions at mantle conditions are possible while still satisfying the laboratory data (Figure 5b). This analysis indicates that the nominal olivine flow law of *Hansen et al.* (2011) may underpredict the contribution of disGBS at mantle conditions.

Our observation of D-type LPO and inference of disGBS at shallow mantle conditions has implications for the acceptable range of flow law parameters. For example, while the deformation mechanism map in Figure 5c satisfies laboratory data (within uncertainty), the disGBS field vanishes for MOR strain rates and is inconsistent with our observation. A grid search over possible flow law parameters reveals a preference for smaller disGBS stress and grain-size exponents n_{GBS} and m_{GBS}, respectively, relative to their nominal reference values (Table S3) and/or a larger dislocation creep stress exponent n_{DISL} (Figure B1; see Appendix B for details). Alternatively, it is possible that the nominal flow law parameter values are valid but mantle grain sizes are smaller than predicted by the wattmeter and/or piezometer due to grain-boundary pinning in the presence of secondary phases such as pyroxene, which is not captured by experiments on pure olivine, a caveat that warrants future exploration.

5.3 Implications for mid-ocean ridge deformation

The strong correspondence between observed anisotropic fast directions and the direction of fossil seafloor spreading at NoMelt implies that the *in situ* elastic tensor represents mantle deformed by corner flow during spreading. Our observations implying shallow deformation via grain-size sensitive disGBS with high strain accumulation (γ = 3–4) and sub-horizontal [100] orientations will inform new geodynamic modeling efforts of MOR dynamics and associated fabric development. Models that assume purely dislocation creep often contain relatively weak anisotropy in the shallow lithosphere with a dipping [100] orientation and A-type LPO (*Blackman et al.*, 1996, 2017), in contrast to what we infer at NoMelt. Girdled fabrics have been previously produced in viscoplastic self-consistent models (*Tommasi et al.*, 2000), but generally such alternative LPO types are not explored in geodynamic models. Our result that D-type LPO prevails in the shallow lithosphere provides a new target for future geodynamic models.

Deformation via disGBS implies a complex non-Newtonian and grain-size dependent rheology that impacts solid-state convection streamlines, melt extraction, and thermal and rheological evolution of the lithosphere and asthenosphere (*Turner et al.*, 2017). Grain size, in particular, has been shown to play an important role in melt focusing near MORs through alteration of the viscosity structure resulting in gradients in compaction pressure (*Turner et al.*, 2015, 2017). Smaller grain sizes in the shallow mantle, such as those we infer, imply decreased porosity and permeability that act as a permeability barrier along which melt may be focused towards the ridge axis. Although we infer deformation dominated by disGBS only in the shallow lithospheric mantle, significantly shallower than where melt is stable off-axis, geodynamic models that include non-Newtonian viscosities predict that disGBS also dominates in the shallow asthenospheric mantle (*Turner et al.*, 2015).

5.4 Limitations and future directions

While this study provides one of the most complete *in situ* elastic models of oceanic lithosphere to date, our approach has limitations. First, we are unable to explicitly solve for fabric dip because only horizontally propagating waves are used. Theoretically, it is possible to utilize P- and S-waves with intermediate incidence angles to constrain fabric dip via the zero-valued off-diagonal elements of eq (2). In practice however, this is extremely challenging and would require earthquake observations from a range of epicentral distances with excellent back-azimuthal coverage to sufficiently sample a wide range

of incidence angles. Ideally, this would be combined with our surface-wave approach in a joint inversion framework. Our use of laboratory data to indirectly infer fabric dip based on the observation of fast azimuth alignment with the FSD suggests fabric is horizontal to within $\sim$10° in our study region, providing confidence in our current approach.

The influence of pyroxene on LPO development, bulk anisotropy, and mantle rheology is still being investigated. A recent study of natural peridotites containing various olivine and orthopyroxene LPO types shows that orthopyroxene has no significant effect on the fast azimuth of seismic anisotropy when olivine composes at least 40% of the sample (*Bernard et al.*, 2021), corroborating our observation in Figure 3f–h. The strength of anisotropy does depend on both the proportion of pyroxene and the magnitude of strain, however (Figure 3a–d). In practice, it is not possible to separate these two effects, and the best one can do is assume a realistic mantle composition based on prior knowledge as we have done. Additionally, shear strain is not readily determined in natural samples except in special cases for which strain markers are present, such as at the Josephine shear zone (*Hansen and Warren*, 2015, *Warren et al.*, 2008), and those samples by definition contain a pre-existing LPO, which also impacts strain development. Untangling these competing effects on anisotropy will require new high-strain experiments using realistic peridotite compositions that examine the effect of olivine and pyroxene together and quantify the influence of pre-existing fabric.

Finally, as our 1-D model represents an average over the 600×400 km NoMelt footprint, we cannot necessarily rule out a variation in LPO type across the region. In particular, a spatial variation from A-type to E-type could appear as D-type LPO when averaged over the array. However, given the relatively simple oceanic setting and minor lateral variations in surface-wave phase velocities at NoMelt (<1%) (*Russell et al.*, 2019), existence of multiple LPO types seems unlikely.

6 Conclusions

We develop the first *in situ* elastic tensor of oceanic lithosphere constrained by co-located shear and compressional observations sensitive to the upper $\sim$7 km of the mantle. By comparing our observation to a suite of previously published tensors from olivine aggregates deformed in nature and in the laboratory, we provide new constraints on LPO type, magnitude of shear strain, and dominant deformation mechanism at MOR conditions. The relatively strong azimuthal anisotropy with fast azimuth parallel to the spreading

direction is consistent with shear strains of 300–400% and sub-horizontal fabric produced by corner flow. The relative strengths of azimuthal and radial anisotropy correspond to D-type LPO ([100] parallel to shear and girdled [001] and [010] perpendicular to shear) irrespective of assumed olivine content or fabric dip. Our observations can be explained by a mantle composition of 60–75% olivine, consistent with observed mantle peridotites, but the competing effects of composition, strain, and pre-existing LPO on anisotropy strength cannot be completely isolated.

D-type LPO is interpreted as evidence for near-ridge deformation dominated by grain-size sensitive disGBS. This implies *in situ* grain sizes of 0.3–15 mm, smaller than predicted by piezometers derived from experiments on pure olivine, which may be the result of grain-boundary pinning by secondary phases such as pyroxene in Earth's interior. Alternatively, the grain-size sensitivity may be underestimated by typical flow laws. We find a slight preference for smaller stress and grain-size exponents in the disGBS flow law and/or a larger stress exponent in the dislocation creep flow law relative to reported experimental values. The grain-size sensitivity of disGBS deformation impacts rheology of the spreading mantle and subsequent LPO development. This study demonstrates the ability to integrate laboratory- and seismological-scale observations of seismic anisotropy to improve understanding of mantle deformation during seafloor spreading.

Appendix

A Wattmeter steady-state grain size calculation

Grain-size evolution as a function of stress (σ) is estimated following the wattmeter approach of *Austin and Evans* (2007):

$$\dot{d} = \frac{K_\mathrm{g}}{p} d^{1-p} \exp\left(-\frac{E_\mathrm{g} + \bar{P}V_\mathrm{g}}{RT}\right) - \frac{2\chi}{c\gamma} d^2 \boldsymbol{\sigma} : \dot{\boldsymbol{\varepsilon}}\,, \tag{3}$$

where K_g and E_g are the grain growth prefactor and activation energy, respectively. The first term on the right-hand side represents grain growth by material diffusion between grains, and the second term represents grain-size reduction through dynamic recrystallization, which depends on χ the fraction of work done by dislocation mechanisms in order to change grain boundary area, average specific grain boundary energy, γ, and a geometric constant, c. We follow (*Behn et al.*, 2009) and assume a grain growth exponent of $p = 3$. Assuming deformation occurs via disGBS, $\dot{\varepsilon} = A_\mathrm{GBS}\sigma^n d^{-m} \exp\left(-(E_\mathrm{GBS} + PV_\mathrm{GBS})/RT\right)$ and setting eq (3) equal to zero, the steady-state grain size is given by:

$$d_\mathrm{ss} = \left[\frac{K_\mathrm{g} c\gamma}{2\chi p A_\mathrm{GBS}\sigma^{n+1}} \exp\left(\frac{(E_\mathrm{GBS} - E_\mathrm{g}) + (PV_\mathrm{GBS} - PV_\mathrm{g})}{RT}\right)\right]^{\frac{1}{1+p-m}} \tag{4}$$

All parameter values can be found in Table S3. The resulting steady-state grain-size variation with stress, or wattmeter, at $T = 1250°\mathrm{C}$ is shown in Figure 5.

B Flow-law uncertainties

Uncertainty in grain-size and stress exponents in olivine flow laws affect both the wattmeter calculation as well as deformation mechanism maps when extrapolated from laboratory to mantle conditions. We evaluate the effect of experimentally determined uncertainties in m_GBS, n_GBS, and n_DISL on the wattmeter and deformation mechanism maps by perturbing them within their uncertainty bounds ($n\pm0.3$ and $m\pm0.1$ relative to the reference values listed in Table S3). In order to remain consistent with the laboratory data, we correspondingly solve for prefactors A_GBS and A_DISL using the strain rate evaluated at a reference state of $d = 60$ μm and $\sigma = 60$ MPa, representative of average laboratory conditions. The deformation mechanism map and wattmeter are then calculated using the new value of A and perturbed values of n

and m. The resulting effects on the deformation mechanism map, and the disGBS region in particular, are shown for two endmember cases in Figure 5b–c. Because we calculate the deformation mechanism maps and the grain size versus stress relationships at a temperature of 1250°C (which is within the temperature range that the grain-growth and deformation experiments were conducted), uncertainties in the activation energies for the flow laws and grain-growth law (*Speciale et al.*, 2020) do not significantly impact our analysis.

We perform a grid search over values of m_{GBS}, n_{GBS}, and n_{DISL} within their uncertainty bounds to determine the range of parameters that satisfy our *in situ* inference of disGBS as well as the laboratory derived grain-size piezometer and wattmeter (Figure B1). A set of parameters is considered acceptable if disGBS is predicted to occur at grain sizes at least as large as those predicted from the piezometer and wattmeter in Figure 5 (i.e., when the piezometer and wattmeter fall completely within the disGBS regime) at mantle strain rates of $10^{-14.5}$–$10^{-12.5}$ s^{-1}. Figure B1 shows that this criterion is met when m_{GBS} and n_{GBS} are smaller than their reference values and/or n_{DISL} is larger than its reference value. Furthermore, there is a clear tradeoff between the disGBS parameters (m_{GBS}, n_{GBS}) and the dislocation creep parameter n_{DISL}.

References

Abramson, E. H., J. M. Brown, L. J. Slutsky, and J. Zaug (1997), The elastic constants of San Carlos olivine to 17 GPa, *Journal of Geophysical Research*, *102*(B6), 12,253–12,263, doi:10.1029/97jb00682.

Austin, N. J., and B. Evans (2007), Paleowattmeters: A scaling relation for dynamically recrystallized grain size, *Geology*, *35*(4), 343–346, doi:10.1130/G23244A.1.

Behn, M. D., G. Hirth, and J. R. Elsenbeck (2009), Implications of grain size evolution on the seismic structure of the oceanic upper mantle, *Earth and Planetary Science Letters*, *282*(1-4), 178–189, doi:10.1016/j.epsl.2009.03.014.

Ben-Ismail, W., and D. Mainprice (1998), An olivine fabric database: An overview of upper mantle fabrics and seismic anisotropy, *Tectonophysics*, *296*(1-2), 145–157, doi:10.1016/S0040-1951(98)00141-3.

Ben-Ismail, W., G. Barruol, and D. Mainprice (2001), The Kaapvaal craton seismic anisotropy: Petrophysical analyses of upper mantle kimberlite nodules, *Geophysical Research Letters*, *28*(13), 2497–2500.

Bernard, R. E., V. Schulte-Pelkum, and W. M. Behr (2021), The competing effects of olivine and orthopyroxene CPO on seismic anisotropy, *Tectonophysics*, *814*, 228,954, doi:10.1016/j.tecto.2021.228954.

Blackman, D. K., J. Kendall, R. D. Paul, H. Wenk, D. Boyce, and J. P. Morgan (1996), Teleseismic imaging of subaxial flow at mid-ocean ridges : traveltime effects of anisotropic mineral texture in the mantle, *Geophysical Journal International*, *127*, 415–426.

Blackman, D. K., D. E. Boyce, O. Castelnau, P. R. Dawson, and G. Laske (2017), Effects of crystal preferred orientation on upper-mantle flow near plate boundaries: Rheologic feedbacks and seismic anisotropy, *Geophysical Journal International*, *210*, 1481–1493, doi:10.1093/gji/ggx251.

Braun, M. G. (2004), Petrologic and microstructural constraints on focused melt transport in dunites and the rheology of the shallow mantle, Ph.D. thesis, Massachesetts Institute of Technology.

Bystricky, M., K. Kunze, L. Burlini, and J. P. Burg (2000), High shear strain of olivine aggregates: Rheological and seismic consequences, *Science*, *290*(5496), 1564–1567, doi:10.1126/science.290.5496.1564.

Carter, N. L., and H. G. Ave'Lallemant (1970), High Temperature Flow of Dunite and Peridotite, *Geological Society of America Bulletin*, *81*(9), 2181–2202, doi:10.1017/CBO9781107415324.004.

Connolly, J. A. (2009), The geodynamic equation of state: What and how, *Geochemistry, Geophysics, Geosystems*, *10*(10), doi:10.1029/2009GC002540.

Dick, H., and J. Natland (1996), Late-Stage Melt Evolution and Transport in the Shallow Mantle beneath the East Pacific Rise, *Proceedings of the Ocean Drilling Program, Scientific Results*, *147*, 103–134, doi:10.2973/odp.proc.sr.147.007.1996.

Dziewonski, A. M., and D. L. Anderson (1981), Preliminary reference Earth model * Adam M., *Physics of the Earth and Planetary Interiors*, *25*, 297–356.

Forsyth, D. W. (1975), The Early Structural Evolution and Anisotropy of the Oceanic Upper Mantle, *Geophysical Journal of the Royal Astronomical Society*, *43*(1), 103–162.

Gaherty, J. B., T. H. Jordan, and L. S. Gee (1996), Seismic structure of the upper mantle in a central Pacific corridor, *Journal of Geophysical Research*, *101*, 22,291–22,309.

Gaherty, J. B., D. Lizarralde, J. A. Collins, G. Hirth, and S. Kim (2004), Mantle deformation during slow seafloor spreading constrained by observations of seismic anisotropy in the western Atlantic, *Earth and Planetary Science Letters*, *228*, 255–265, doi:10.1016/j.epsl.2004.10.026.

Hacker, B. R. (2008), H2O subduction beyond arcs, *Geochemistry, Geophysics, Geosystems*, *9*(3), doi:10.1029/2007GC001707.

Hansen, L. N., and J. M. Warren (2015), Quantifying the effect of pyroxene on deformation of peridotite in a natural shear zone, *Journal of Geophysical Research: Solid Earth*, *120*, 2717–2738, doi:10.1002/2014JB011584.Received.

Hansen, L. N., M. E. Zimmerman, and D. L. Kohlstedt (2011), Grain boundary sliding in San Carlos olivine: Flow law parameters and crystallographic-preferred orientation, *Journal of Geophysical Research: Solid Earth*, *116*(8), 1–16, doi:10.1029/2011JB008220.

Hansen, L. N., Y. H. Zhao, M. E. Zimmerman, and D. L. Kohlstedt (2014), Protracted fabric evolution in olivine: Implications for the relationship among strain, crystallographic fabric, and seismic anisotropy, *Earth and Planetary Science Letters*, *387*, 157–168, doi:10.1016/j.epsl.2013.11.009.

Hansen, L. N., J. M. Warren, M. E. Zimmerman, and D. L. Kohlstedt (2016), Viscous anisotropy of textured olivine aggregates, Part 1: Measurement of the magnitude and evolution of anisotropy, *Earth and Planetary Science Letters*, *445*, 92–103, doi:10.1016/j.epsl.2016.04.008.

Hansen, L. N., M. Faccenda, and J. M. Warren (2021), A review of mechanisms generating seismic anisotropy in the upper mantle, *Physics of the Earth and Planetary Interiors*, *313*, 106,662, doi:10.1016/j.pepi.2021.106662.

Hess, H. (1964), Seismic Anisotropy of the Uppermost Mantle under Oceans, *Nature*, *203*, 629–631.

Hirth, G., and D. L. Kohlstedt (2003), Rheology of the Upper Mantle and the Mantle Wedge: A View from the Experimentalists, in *Inside the Subduction Factory: Geophysical Monograph 138*, pp. 83–105.

Hirth, G., and D. L. Kohlstedt (2015), The stress dependence of olivine creep rate: Implications for extrapolation of lab data and interpretation of recrystallized grain size, *Earth and Planetary Science Letters*, *418*, 20–26, doi:10.1016/j.epsl.2015.02.013.

Jung, H., and S.-i. Karato (2001), Water-Induced Fabric Transitions in Olivine, *Science*, *293*, 1460–1464.

Jung, H., I. Katayama, Z. Jiang, T. Hiraga, and S.-i. Karato (2006), Effect of water and stress on the lattice-preferred orientation of olivine, *Tectonophysics*, *421*, 1–22, doi:10.1016/j.tecto.2006.02.011.

Karato, S.-i. (2008), Insights into the nature of plume-asthenosphere interaction from central Pacific geophysical anomalies, *Earth and Planetary Science Letters*, *274*, 234–240, doi:10.1016/j.epsl.2008.07.033.

Karato, S.-i., and P. Wu (1993), Rheology of the upper mantle: a synthesis., doi:10.1126/science.260.5109.771.

Karato, S.-i., M. Toriumi, and T. Fujii (1980), Dynamic recrystallization of olivine single crystals during high-temperature creep, *Geophysical Research Letters*, *7*(9), 649–652.

Karato, S.-i., H. Jung, I. Katayama, and P. Skemer (2008), Geodynamic Significance of Seismic Anisotropy of the Upper Mantle : New Insights from Laboratory Studies, *Annual Review Earth and Planetary Sciences*, *36*, 59–95, doi:10.1146/annurev.earth.36.031207.124120.

Katayama, I., H. Jung, and S.-i. Karato (2004), New type of olivine fabric from deformation experiments at modest water content and low stress, *Geology*, *32*(12), 1045–1048, doi:10.1130/G20805.1.

Lin, P.-Y. P., J. B. Gaherty, G. Jin, J. A. Collins, D. Lizarralde, R. L. Evans, and G. Hirth (2016), High-resolution seismic constraints on flow dynamics in the oceanic asthenosphere, *Nature*, *535*(7613), 1–9, doi:10.1038/nature18012.

Mark, H. F., D. Lizarralde, J. A. Collins, N. C. Miller, G. Hirth, J. B. Gaherty, and R. L. Evans (2019), Azimuthal Seismic Anisotropy of 70-Ma Pacific-Plate Upper Mantle, *Journal of Geophysical Research: Solid Earth*, *124*, 1889–1909, doi:10.1029/2018JB016451.

Mehl, L., B. Hacker, G. Hirth, and P. B. Kelemen (2003), Arc-parallel flow within the mantle wedge: Evidence from the accreted Talkeetna arc, south central Alaska, *Journal of Geophysical Research*, *108*(B8), doi:10.1029/2002jb002233.

Michibayashi, K., T. Ina, and K. Kanagawa (2006), The effect of dynamic recrystallization on olivine fabric and seismic anisotropy: Insight from a ductile shear zone, Oman ophiolite, *Earth and Planetary Science Letters*, *244*, 695–708, doi:10.1016/j.epsl.2006.02.019.

Michibayashi, K., D. Mainprice, A. Fujii, S. Uehara, Y. Shinkai, Y. Kondo, Y. Ohara, T. Ishii, P. Fryer, S. H. Bloomer, A. Ishiwatari, J. W. Hawkins, and S. Ji (2016), Natural olivine crystal-fabrics in the western Pacific convergence region : A new method to identify fabric type, *Earth and Planetary Science Letters*, *443*, 70–80, doi:10.1016/j.epsl.2016.03.019.

Montagner, J. P., and H. C. Nataf (1986), A simple method for inverting the azimuthal anisotropy of surface waves, *Journal of Geophysical Research*, *91*, 511–520.

Montagner, J. P., and T. Tanimoto (1991), Global Upper Mantle Tomography of Seismic Velocities and Anisotropies, *JGR*, *96*(9), 20,337–20,351.

Nishimura, C. E., and D. W. Forsyth (1989), The Anisotropic Structure of the Upper Mantle in the Pacific Ocean, *Geophysical Journal of the Royal Astronomical Society*, *96*(2), 203–229.

Niu, Y., and R. Hékinian (1997), Basaltic liquids and harzburgitic residues in the Garrett Transform: A case study at fast-spreading ridges, *Earth and Planetary Science Letters*, *146*, 243–258, doi:10.1016/s0012-821x(96)00218-x.

Peselnick, L., and A. Nicolas (1978), Seismic Anisotropy in an Ophiolite Peridotite: Application to Oceanic Upper Mantle, *Journal of Geophysical Research*, *83*(B3), 1227–1235.

Qi, C., L. N. Hansen, D. Wallis, B. K. Holtzman, and D. L. Kohlstedt (2018), Crystallographic Preferred Orientation of Olivine in Sheared Partially Molten Rocks: The Source of the a-c Switch, *Geochemistry, Geophysics, Geosystems*, *19*, 316–336, doi:10.1002/2017GC007309.

Russell, J. B., J. B. Gaherty, P. Y. P. Lin, D. Lizarralde, J. A. Collins, G. Hirth, and R. L. Evans (2019), High-Resolution Constraints on Pacific Upper Mantle Petrofabric Inferred From Surface-Wave Anisotropy, *Journal of Geophysical Research: Solid Earth*, *124*, 631–657, doi:10.1029/2018JB016598.

Satsukawa, T., K. Michibayashi, U. Raye, E. Y. Anthony, J. Pulliam, and R. Stern (2010), Uppermost mantle anisotropy beneath the southern Laurentian margin: Evidence from Knippa peridotite xenoliths, Texas, *Geophysical Research Letters*, *37*, L20,312, doi:10.1029/2010GL044538.

Skemer, P., J. M. Warren, P. B. Kelemen, and G. Hirth (2010), Microstructural and rheological evolution of a mantle shear zone, *Journal of Petrology*, *51*(1-2), 43–53, doi:10.1093/petrology/egp057.

561 Skemer, P., J. M. Warren, and G. Hirth (2012), The influence of deformation history on the interpretation
562 of seismic anisotropy, *Geochemistry, Geophysics, Geosystems*, *13*(3), 1–10, doi:10.1029/2011GC003988.

563 Speciale, P. A., W. M. Behr, G. Hirth, and L. Tokle (2020), Rates of Olivine Grain Growth During
564 Dynamic Recrystallization and Postdeformation Annealing, *Journal of Geophysical Research: Solid*
565 *Earth*, *125*(11), doi:10.1029/2020JB020415.

566 Stixrude, L., and C. Lithgow-Bertelloni (2011), Thermodynamics of mantle minerals - II. Phase equilibria,
567 *Geophysical Journal International*, *184*(3), 1180–1213, doi:10.1111/j.1365-246X.2010.04890.x.

568 Takeo, A., H. Kawakatsu, T. Isse, K. Nishida, H. Shiobara, H. Sugioka, A. Ito, and H. Utada (2018),
569 In Situ Characterization of the Lithosphere-Asthenosphere System beneath NW Pacific Ocean Via
570 Broadband Dispersion Survey With Two OBS Arrays, *Geochemistry, Geophysics, Geosystems*, *19*,
571 doi:10.1029/2018GC007588.

572 Tommasi, A. (1998), Forward modeling of the development of seismic anisotropy in the upper mantle,
573 *Earth and Planetary Science Letters*, *160*, 1–13.

574 Tommasi, A., D. Mainprice, G. Canova, and Y. Chastel (2000), Viscoplastic self-consistent and
575 equilibrium-based modeling of olivine lattice preferred orientations: Implications for the upper mantle
576 seismic anisotropy, *Journal of Geophysical Research*, *105*, 7893–7908.

577 Toomey, D. R., D. Jousselin, R. A. Dunn, W. S. D. Wilcock, and R. S. Detrick (2007), Skew of mantle
578 upwelling beneath the East Pacific Rise governs segmentation, *Nature*, *446*, 409–414, doi:10.1038/
579 nature05679.

580 Turner, A. J., R. F. Katz, and M. D. Behn (2015), Grain-size dynamics beneath mid-ocean ridges:
581 Implications for permeability and melt extraction, *Geochemistry, Geophysics, Geosystems*, *16*, 925–
582 946, doi:10.1002/2014GC005692.Received.

583 Turner, A. J., R. F. Katz, M. D. Behn, and T. Keller (2017), Magmatic Focusing to Mid-Ocean Ridges:
584 The Role of Grain-Size Variability and Non-Newtonian Viscosity, *Geochemistry, Geophysics, Geosys-*
585 *tems*, *18*(12), 4342–4355, doi:10.1002/2017GC007048.

586 Walker, A. M., and J. Wookey (2012), Computers & Geosciences MSAT A new toolkit for the analysis of
587 elastic and seismic anisotropy, *Computers and Geosciences*, *49*, 81–90, doi:10.1016/j.cageo.2012.05.031.

Warren, J. M. (2016), Global variations in abyssal peridotite compositions, *Lithos*, *248-251*, 193–219, doi:10.1016/j.lithos.2015.12.023.

Warren, J. M., G. Hirth, and P. B. Kelemen (2008), Evolution of olivine lattice preferred orientation during simple shear in the mantle, *Earth and Planetary Science Letters*, *272*(3-4), 501–512, doi:10.1016/j.epsl.2008.03.063.

Zhang, S., and S.-i. Karato (1995), Lattice preferred orientation of olivine aggregates deformed in simple shear, *Nature*, *375*, 774–777.

Zhang, S., S. ichiro Karato, J. Fitz Gerald, U. H. Faul, and Y. Zhou (2000), Simple shear deformation of olivine aggregates, *Tectonophysics*, *316*, 133–152, doi:10.1016/S0040-1951(99)00229-2.

Acknowledgments

The authors thank Haemyeong Jung, Katsuyoshi Michibayashi, and Misha Bystricky who shared previously published elastic tenors used in this study. This work was supported by the NSF under Grant No. OCE-0928270 and OCE-1538229 (J.B. Gaherty).

Data Availability Statement

Seismic data was accessed through the IRIS Data Management Center under network code ZA using the open-source Python package ObsPy (`https://docs.obspy.org/`). The complete elastic model NoMelt_SPani is included in the Supplementary Material. Elastic tensors were manipulated and visualized using the MATLAB Seismic Anisotropy Toolkit (`https://geophysics.gly.bris.ac.uk/MSAT/`).

Supplementary materials

Figs. S1 to S6

Tables S1 to S3

Figures

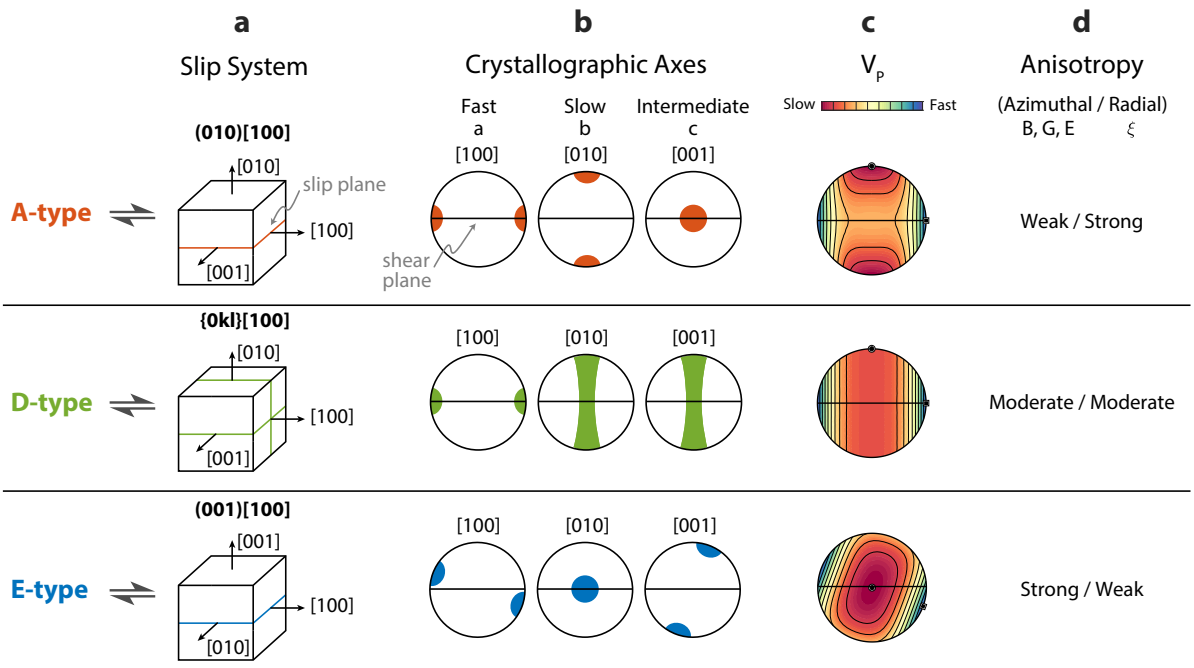

Figure 1: **Summary of the most commonly observed LPO types.** Schematic showing the **a** slip systems, **b** crystallographic orientations, **c** compressional velocities V_P, and **d** relative strengths of radial and azimuthal anisotropy for A-, D-, and E-type fabrics under the assumption that the shear plane is parallel to Earth's surface. Note the qualitative differences in V_P between the three fabric types arising from the relative orientations of [100], [010], and [001]. Variations in the slow [010] and intermediate [001] axes result in measurable differences in seismic anisotropy. Azimuthal anisotropy is sensitive to the two crystallographic axes in the horizontal plane, and radial anisotropy is sensitive to the difference between the azimuthally averaged horizontal axes and the vertically oriented axis.

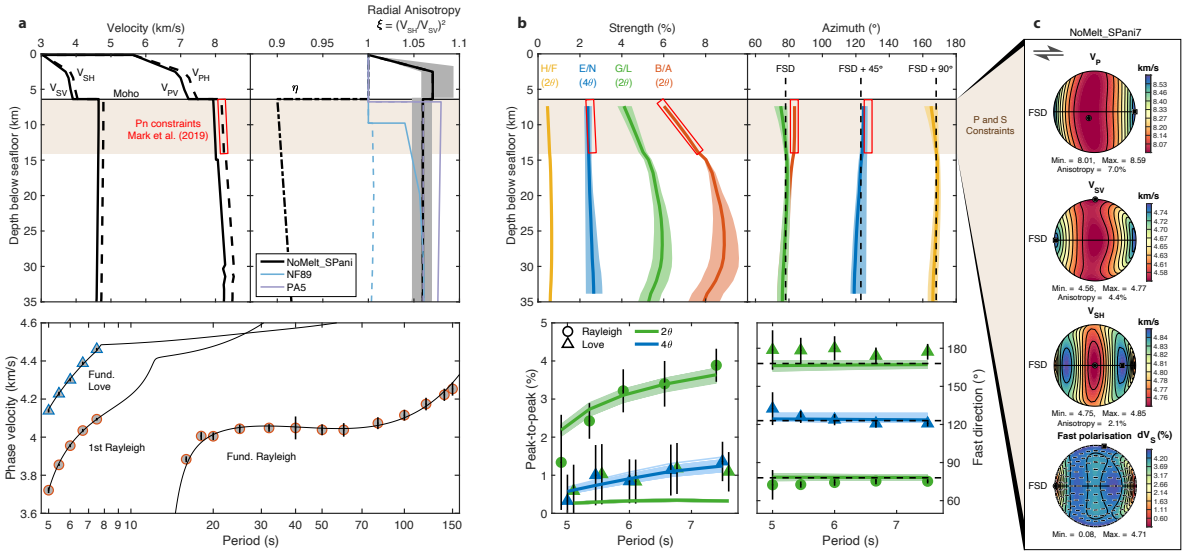

Figure 2: **Comprehensive elastic model and data fit for the NoMelt region.** Summary of the NoMelt_SPani model. **a**, V_P, V_S, and Radial anisotropy model and data fit after (*Russell et al.*, 2019). Grey shading for NoMelt radial anisotropy captures the range of models that fit the data, with the best fit model shown in black. Brown shading indicates where both V_P (*Mark et al.*, 2019) and V_S constraints exist in the upper ∼7 km of the mantle. NF89, (*Nishimura and Forsyth*, 1989) 52–110 Ma region; PA5, (*Gaherty et al.*, 1996). **b**, Azimuthal anisotropy strength and azimuth. Model uncertainties of two standard deviations from bootstrapping are shaded. Data fit and range of bootstrap model fits are shown in the lower panels. **c**, Velocity calculations for the average elastic tensor for the upper ∼7 km of the lithospheric mantle (NoMelt_SPani7), plotted using the MATLAB Seismic Anisotropy Toolkit (*Walker and Wookey*, 2012). The horizontal black line denotes the horizontal plane with the fossil-spreading direction (FSD) to the east and west. Maxima and minima are denoted by a square and circle, respectively. $dV_S = 200(V_{SH} - V_{SV})/(V_{SH} + V_{SV})$

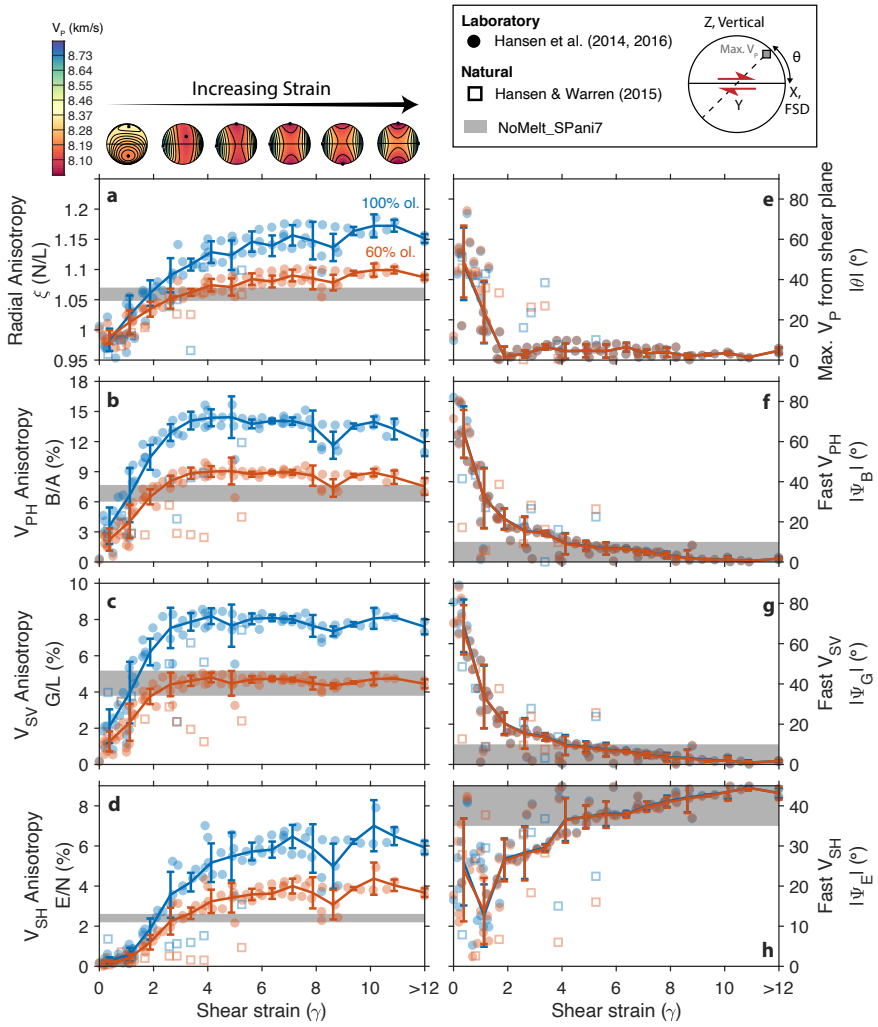

Figure 3: **NoMelt anisotropy compared with olivine petrofabric data as a function of shear strain and pyroxene content.** Anisotropy strength (**a**–**d**) and fast azimuth with respect to the shear direction or FSD (**f**–**h**) for laboratory (solid circles) (*Hansen et al.*, 2014, 2016) and natural samples (open squares) (*Hansen and Warren*, 2015). The NoMelt seismic model for the upper ∼7 km of the lithospheric mantle is shown in grey with a width that represents the full range of values in that depth range. NoMelt FSD uncertainty is ∼10°. **e** Magnitude of the angle between maximum V_P and the shear plane; seismic model does not constrain this parameter. Calculations for (blue) pure olivine and (red) 60% olivine, 40% orthopyroxene are shown (see Methods for details on the inclusion of orthopyroxene). Error bars show median and standard deviation for laboratory data binned by strain with bin width $\gamma = 0.75$. V_P surfaces are shown above **a** for laboratory samples averaged by increments of $\gamma = 2$ (See also Figure S6). All samples oriented consistent with the seismic reference frame: shear plane parallel to Earth's surface and shear direction parallel to the FSD.

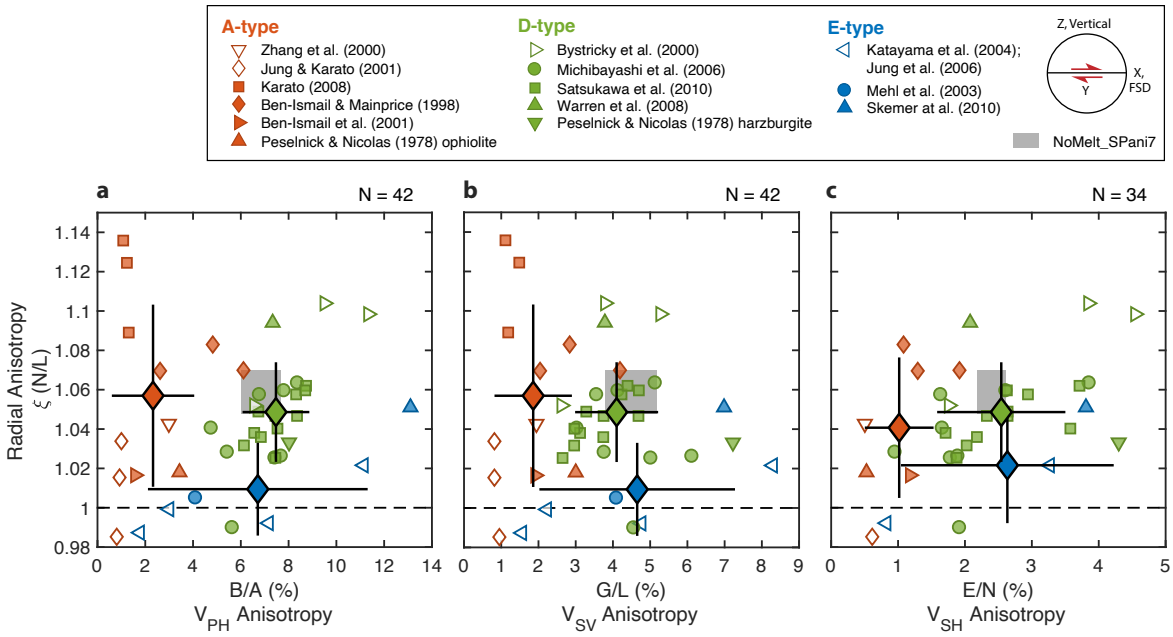

Figure 4: **Anisotropy of A-, D-, and E-type olivine LPO.** Radial anisotropy compared to **a** V_{PH}, **b** V_{SV}, and **c** V_{SH} azimuthal anisotropy for three fabric types compared to the NoMelt model, shown in grey. Open and closed symbols denote laboratory and natural samples, respectively. The large filled diamonds show the mean and one standard deviation for each fabric type. Effects of orthopyroxene are included assuming a composition of 75% olivine and 25% orthopyroxene by volume. No correction is applied to the samples from *Peselnick and Nicolas* (1978), which were derived ultrasonically and therefore already include the bulk chemistry. Note that **c** contains fewer data points than **a** and **b** due unreported V_{SH} anisotropy values for some studies.

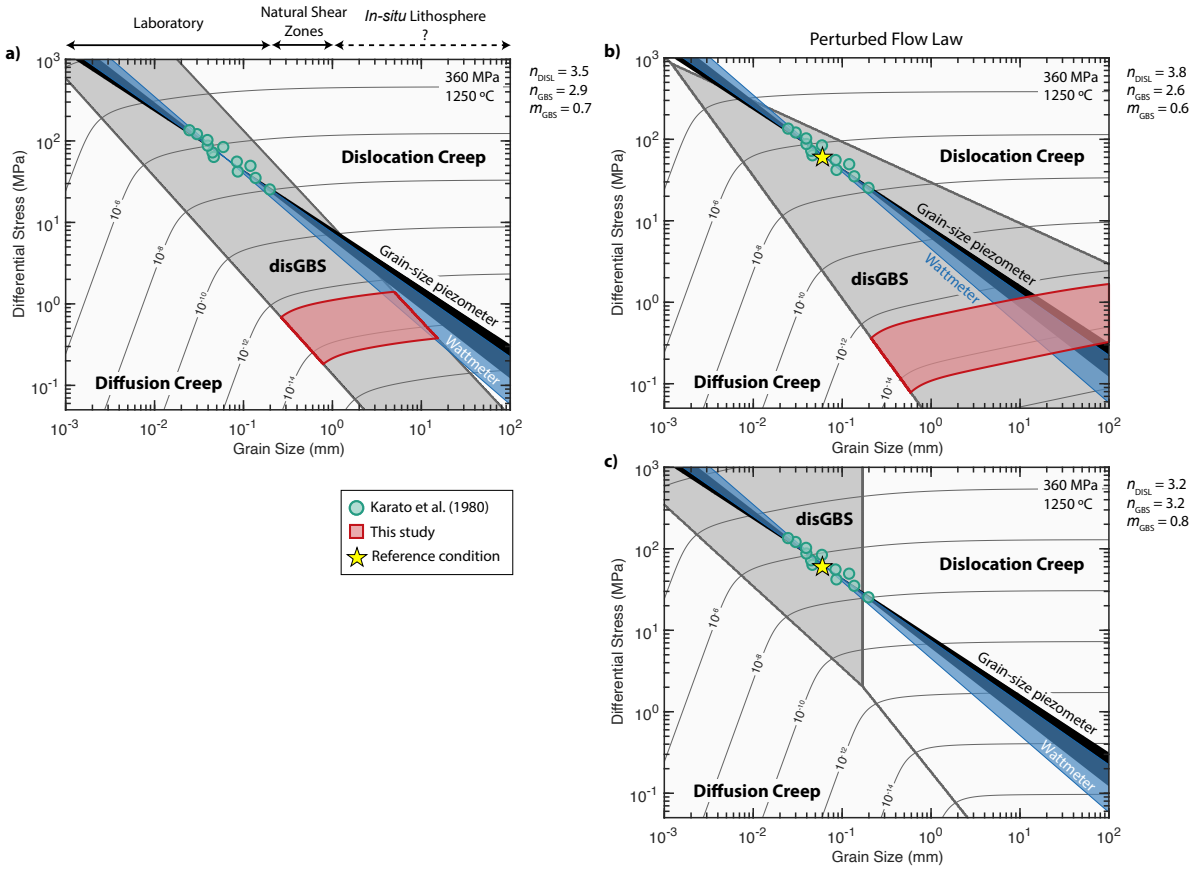

Figure 5: **Deformation mechanism maps at mid-ocean ridge conditions. a** Strain rate contours are calculated using the nominal olivine flow laws of *Hansen et al.* (2011) at a temperature of 1250°C and pressure of 360 MPa (see Table S3), approximating shallow mantle conditions at the MOR. The red region bounded by strain rates of $10^{-14.5}$–$10^{-12.5}$ s^{-1} and within the grey dislocation-accomodated grain boundary sliding (disGBS) regime represents the range of stress and grain sizes consistent with the observation of D-type LPO. The grain-size wattmeter of *Austin and Evans* (2007) is shown in blue and includes uncertainties in laboratory derived stress and grain-size exponents (see Methods for details). A commonly used grain-size piezometer (*Hirth and Kohlstedt*, 2015, *Karato et al.*, 1980) is shown in black. Laboratory data of *Karato et al.* (1980) are shown in teal. **b**–**c** same as a) but for perturbed flow law parameters n_{DISL}, n_{GBS}, and m_{GBS} within their uncertainty bounds, representing endmember cases. The star marks the reference state ($d = 60$ μm, $\sigma = 60$ MPa) used to ensure agreement with laboratory data (See methods for details). In c), the disGBS region vanishes for realistic MOR strain rates, and therefore is not supported by our observation.

Table 1: NoMelt_SPani7 elastic tensor, C_{ij}, averaged over the upper ∼7km of the mantle. The tensor is oriented in the seismological reference frame with X parallel to the fossil-spreading direction, Y parallel to Earth's surface and perpendicular to fossil spreading, and Z perpendicular to Earth's surface.

i	j	1	2	3	4	5	6
1		243.5427	71.5726	73.6646	0	0	1.5311
2		–	212.0492	74.4322	0	0	1.2569
3		–	–	213.2303	0	0	0.0068
4		–	–	–	68.5948	-0.0441	0
5		–	–	–	–	75.3675	0
6		–	–	–	–	–	74.4751

Appendix Figures

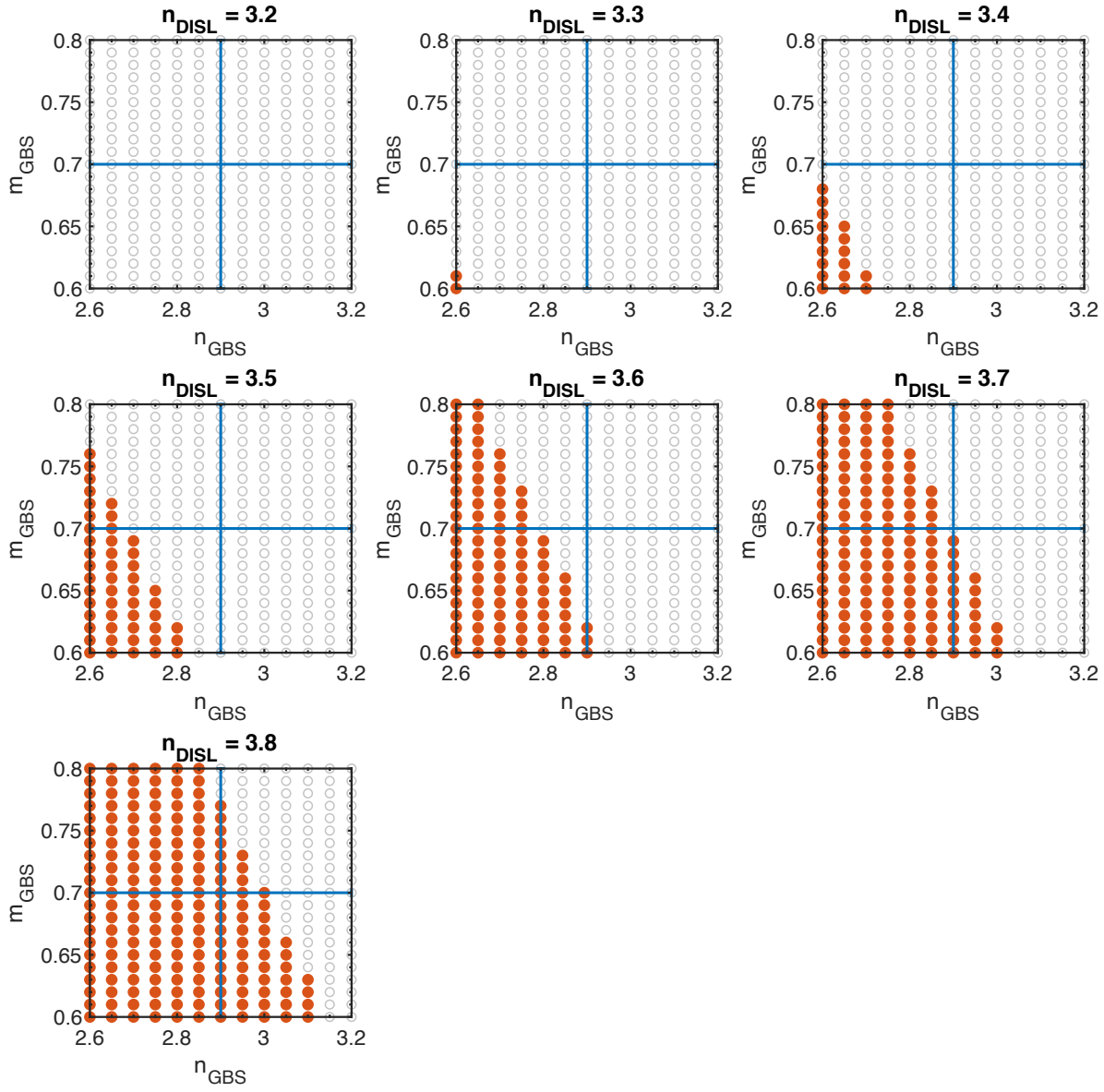

Figure B1: **Flow law parameter combinations which predict disGBS at mantle strain rates.** A grid search is performed over values of n_{DISL}, n_{GBS}, and m_{GBS} within their uncertainty bounds in order to determine the combinations for which disGBS is predicted to occur at grain sizes corresponding to the piezometer and wattmeter shown in Figure 5 at mantle strain rates. A combination of parameters is considered acceptable when the grain-size piezometer and wattmeter are completely within the disGBS region of the deformation mechanism map for strain rates of $10^{-14.5}$–$10^{-12.5}$ s^{-1}. Filled red circles indicate parameter combinations for which this criterion is met, while open circles failed to meet this criterion. The vertical and horizontal blue lines indicate the reference values of n_{GBS} and m_{GBS}, respectively from Table S3. The reference value of n_{DISL} is 3.5. We find that smaller values of n_{GBS} and m_{GBS} and/or larger values n_{DISL} relative to their reference values are favorable.

Supplementary Figures and Tables

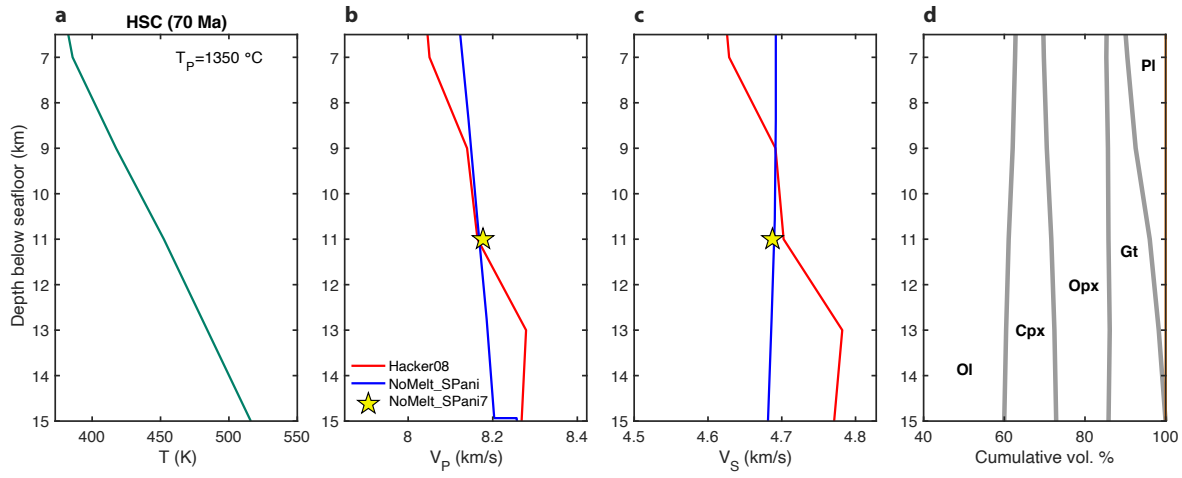

Figure S1: **Estimating V_P, V_S, and olivine content. a** 70 Ma half-space cooling (HSC) geotherm with mantle potential temperature $T_P = 1350°$C. **b, c** Mineral physics calculations of Voigt average V_P and V_S (red solid lines) and **d** mineral abundance from Perple_X (*Connolly*, 2009), using the solution models of *Stixrude and Lithgow-Bertelloni* (2011) and assuming a depleted mid-ocean ridge basalt (MORB) mantle composition (*Hacker*, 2008). The average velocities for the upper 7 km, NoMelt_SPani7, is indicated by the yellow star. Although the predicted velocity gradients are less steep for both V_P and V_S (and for V_P, opposite in sign), there is fair agreement with the depth averaged NoMelt velocities. Modal estimates yield ∼60% olivine. Ol = olivine; Cpx = clinopyroxene; Opx = orthopyroxene; Gt = garnet; Pl = plagioclase

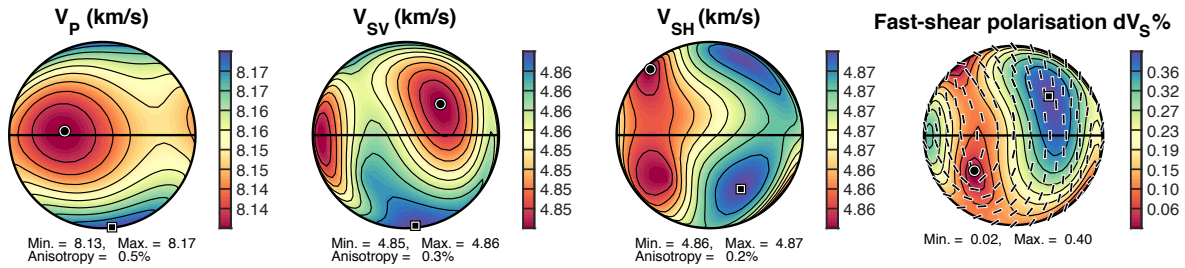

Figure S2: **Orthopyroxene texture used in calculations.** A generic orthopyroxene texture from the torsion experiments of *Hansen et al.* (2014). The fabric is extremely weak ($\sim$0.4% V_{P} anisotropy) and oriented with its [100] crystallographic axis perpendicular to the shear plane, [001] sub-parallel to the shear direction, and [010] perpendicular to shear and in the shear plane. $dV_{\mathrm{S}} = 200(V_{\mathrm{SH}} - V_{\mathrm{SV}})/(V_{\mathrm{SH}} + V_{\mathrm{SV}})$

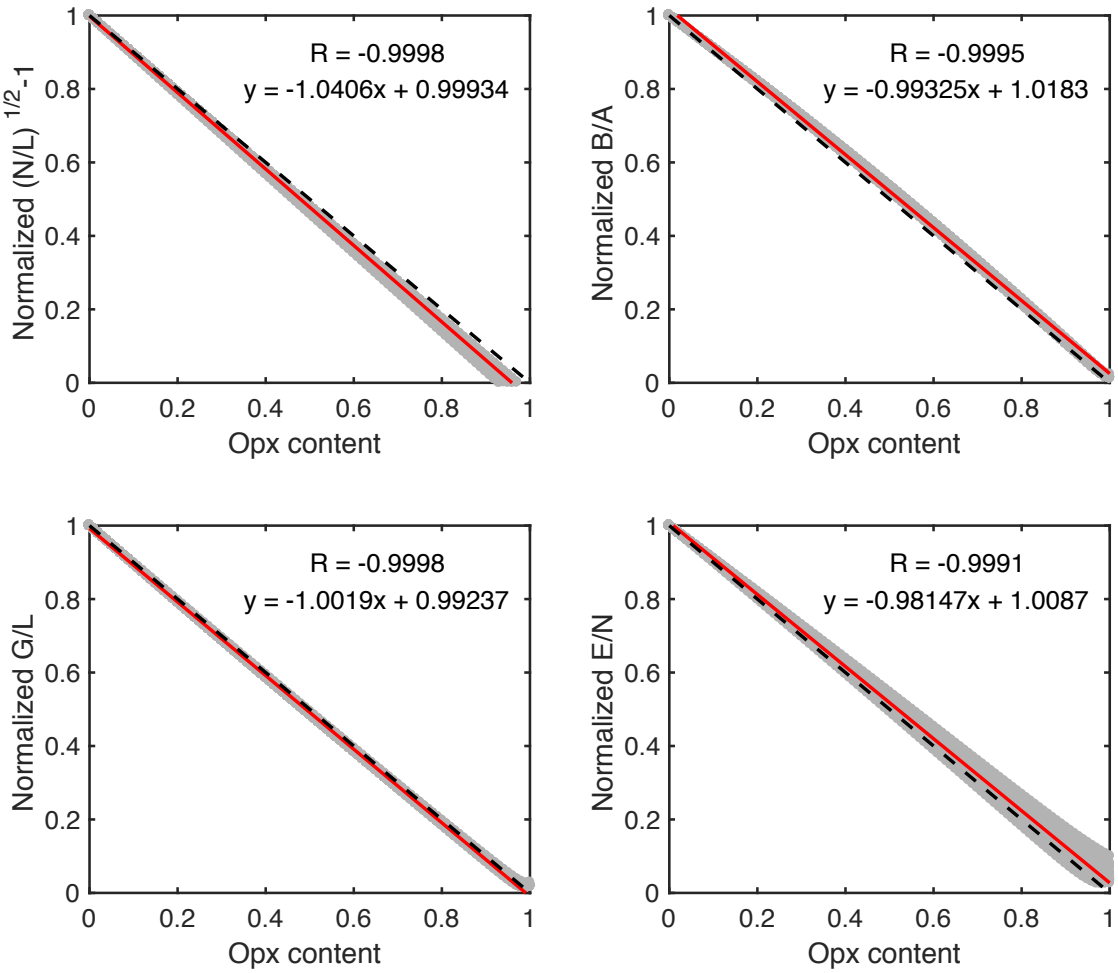

Figure S3: **Reduction in anisotropy strength with increasing orthopyroxene content.** Using well-developed laboratory olivine samples from *Hansen et al.* (2014, 2016) with shear strains of $\gamma > 2$, shown in grey, scaling relationships are found between orthopyroxene content and anisotropy strength (using the orthopyroxene fabric in Figure S2; see methods for details). Anisotropy values for each sample are normalized by the pure olivine estimate in order to determine a single scaling relation for all samples. The best fit line that describes anisotropy reduction with increasing orthopyroxene is shown in red, and nearly falls along the -1:1 line dashed in black.

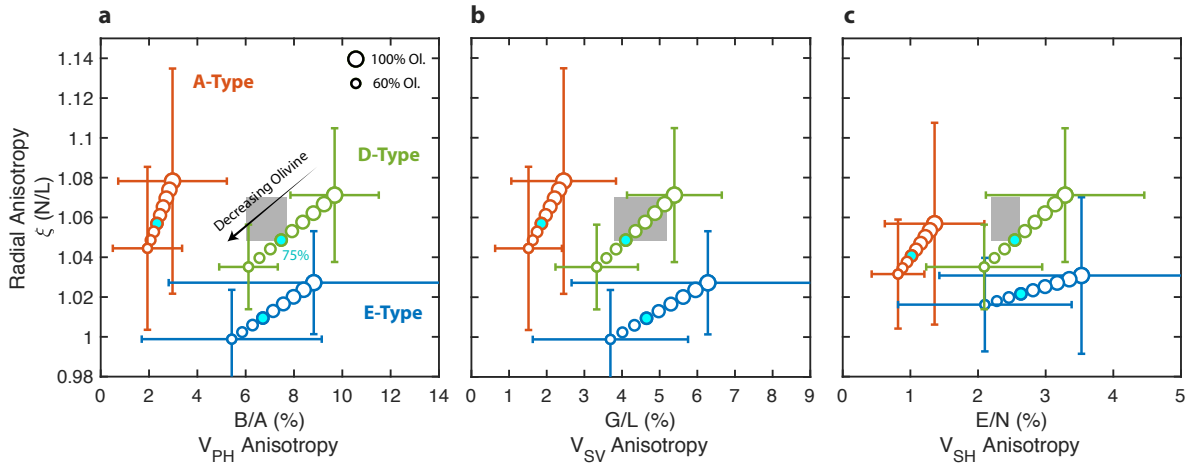

Figure S4: **Effect of assumed olivine content on LPO-type comparison. a–c**, As in Figure 4 in the main text. Circles show anisotropy averages assuming varying ratios of olivine and pyroxene content, where symbol size scales with the amount of olivine ranging from 60% to 100% in increments of 5%, and color denotes fabric type. Anisotropy strength decreases with decreasing olivine content. The best fitting composition of 75% olivine and 25% is shown in cyan.

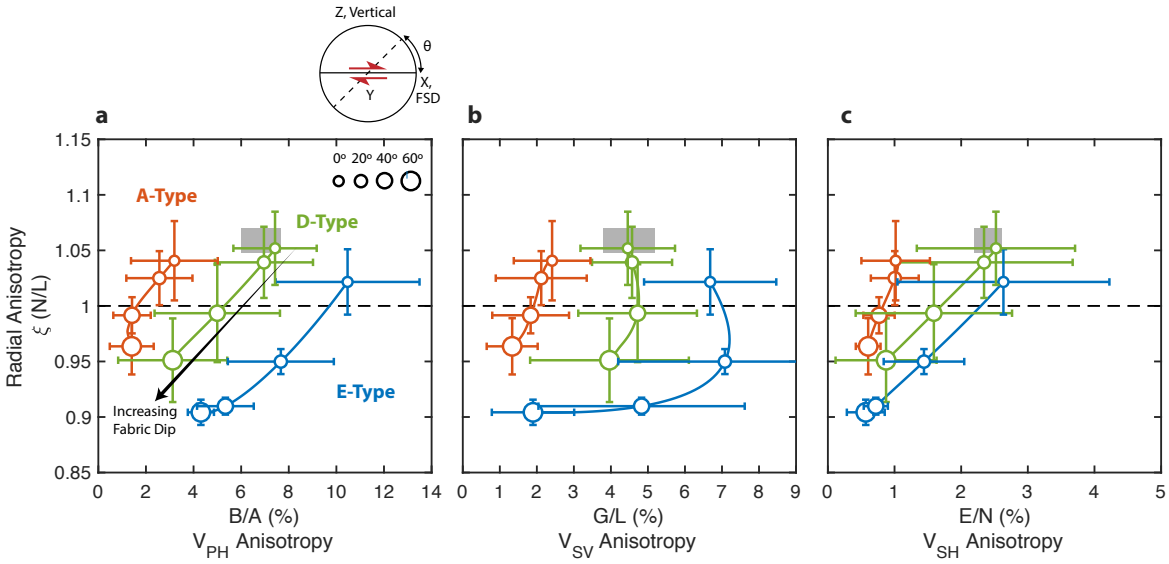

Figure S5: **Effect of fabric dip on LPO-type comparison. a–c**, As in Figure 4 in the main text. Symbols show anisotropy averages and one standard deviation after rotating samples about the Y axis by an angle θ, effectively rotating [100] out of the shear plane. Symbol size scales with introduced fabric dip ranging from 0° to 60°, and color denotes fabric type. A composition of 75% olivine and 25% orthopyroxene is assumed. Radial and azimuthal anisotropy generally decreases with increasing fabric dip. In detail, V_{SV} anisotropy in **b** shows a more complex behavior, in particular for samples with strong azimuthal anisotropy, where an initial slight increase with dip to 20-40° is followed by a nonlinear decrease.

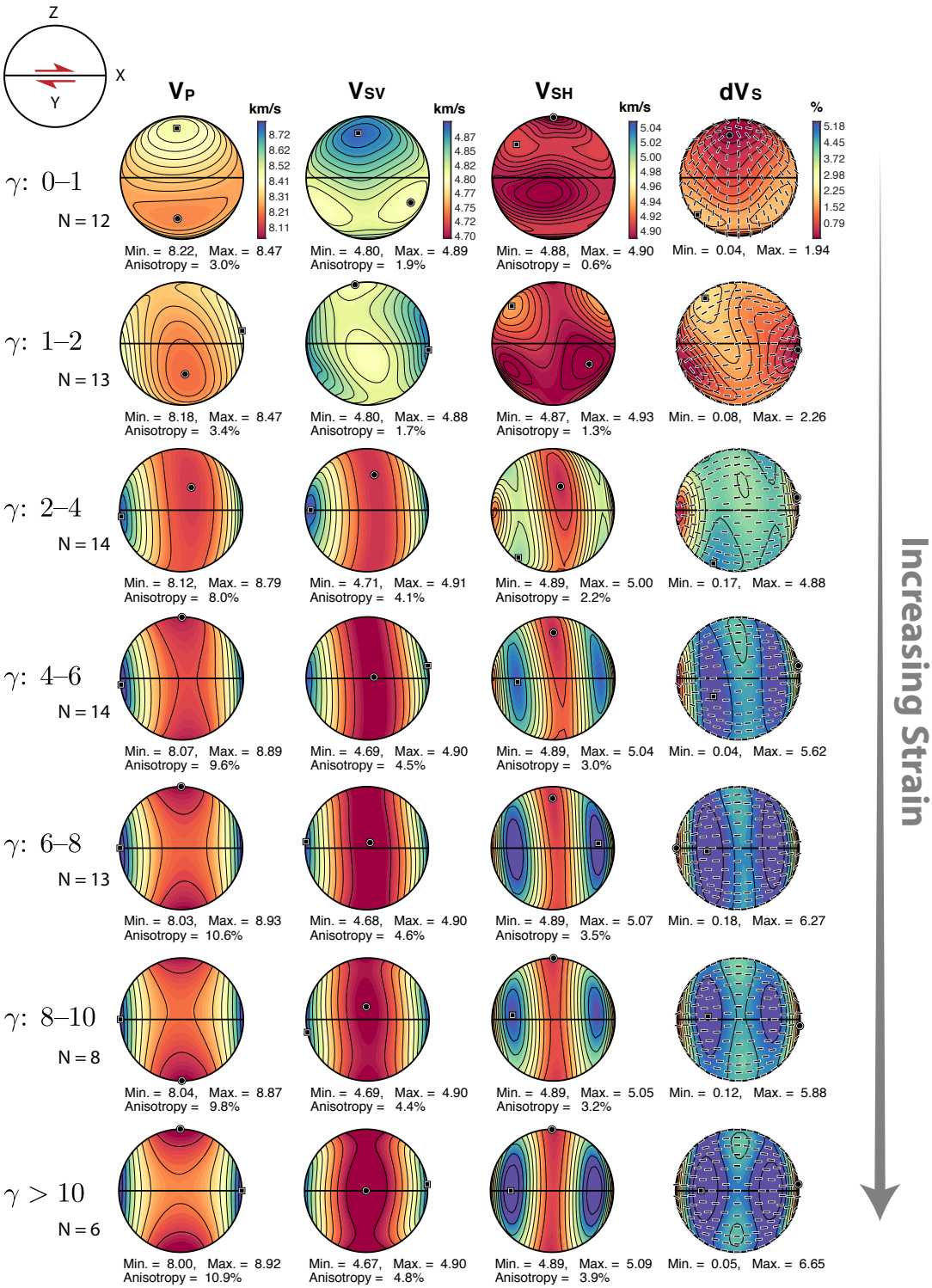

Figure S6: **Strain evolution of anisotropy for laboratory samples shown in Figure 3.** (left to right) Columns show V_P, V_{SV}, V_{SH}, and dV_S anisotropy for laboratory samples from *Hansen et al.* (2014, 2016) grouped and averaged by shear strain for 60% olivine and 40% pyroxene. (top to bottom) Each row represents an average of all samples within the range of γ indicated at the left of each row. Strain increases from top to bottom. A common color scale is used for each column. $dV_S = 200(V_{SH} - V_{SV})/(V_{SH} + V_{SV})$

Table S1: NoMelt_SPani transversely isotropic velocity model with depth relative to sea surface.

Depth (km)	V_{SV} (km/s)	V_{SH} (km/s)	V_{PV} (km/s)	V_{PH} (km/s)	η	ρ (g cm^{-3})
0.000	0.000	0.000	1.500	1.500	1.00	1.030
5.225	0.000	0.000	1.500	1.500	1.00	1.030
5.225	0.150	0.150	1.900	1.900	1.00	1.500
5.375	0.150	0.150	1.900	1.900	1.00	1.500
5.375	3.046	3.046	5.635	5.635	1.00	3.027
7.750	3.699	3.828	6.844	7.082	1.00	3.027
8.626	3.783	3.915	6.999	7.242	1.00	3.027
10.300	3.842	3.976	7.108	7.355	1.00	3.027
11.610	3.906	4.042	7.227	7.478	1.00	3.027
11.610	4.646	4.783	7.934	8.168	0.90	3.339
13.600	4.646	4.783	7.955	8.189	0.90	3.340
15.790	4.644	4.781	7.975	8.210	0.90	3.341
17.980	4.640	4.777	7.997	8.232	0.90	3.342
20.160	4.635	4.772	8.014	8.250	0.90	3.343
20.160	4.635	4.772	8.066	8.303	0.90	3.343
23.870	4.627	4.764	8.119	8.358	0.91	3.346
25.725	4.623	4.760	8.146	8.385	0.91	3.347
27.580	4.619	4.755	8.171	8.412	0.91	3.349
29.435	4.614	4.751	8.198	8.439	0.91	3.350

Table S2: NoMelt_SPani azimuthal anisotropy model with depth relative to sea surface.

Depth (km)	G/L (%)	Ψ_{G} (°)	B/A (%)	Ψ_{B} (°)	E/N (%)	Ψ_{E} (°)	H/F (%)	Ψ_{H} (°)
13.600	4.25	75.69	6.28	83.35	2.38	124.61	0.47	165.53
15.790	4.56	76.93	6.85	83.34	2.39	124.41	0.50	166.72
17.980	4.86	77.90	7.38	83.17	2.40	124.07	0.53	167.70
20.160	5.27	78.80	8.01	82.18	2.42	123.29	0.58	168.67
23.870	5.61	78.90	8.46	80.50	2.46	122.25	0.62	168.79
25.725	5.73	78.74	8.62	79.73	2.48	121.75	0.63	168.67
27.580	5.83	78.45	8.76	78.92	2.51	121.18	0.64	168.41
29.435	5.90	78.06	8.85	78.23	2.53	120.67	0.65	168.04

Table S3: Nominal flow law and grain-size evolution parameters used to calculate the wattmeter and deformation mechanism maps

Symbol	Description	Value	Units
R	gas constant	8.314	J mol^{-1} K^{-1}
T	temperature	1523	K
P	pressure	360	MPa
G_0	dry grain growth rate constant	1.5×10^{-5}	m^p s^{-1}
E_g	activation energy for grain growth	350	kJ mol^{-1}
V_g	activation volume for grain growth	8×10^{-6}	m^3 mol^{-1}
p	grain growth exponent	3	
χ	fraction of work done by dislocation mechanisms	0.03	
γ	average specific grain boundary energy	1	J m^{-2}
c	geometric constant	3	
n_{GBS}	disGBS stress exponent	2.9	
m_{GBS}	disGBS grain-size exponent	0.7	
A_{GBS}	disGBS prefactor	$10^{4.8}$	μm$^{-0.7}$ MPa$^{-2.9}$ s^{-1}
E_{GBS}	disGBS activation energy	4.45×10^5	J mol^{-1}
V_{GBS}	disGBS activation volume	1.5×10^{-5}	m^3 mol^{-1}
n_{DISL}	dislocation creep stress exponent	3.5	
m_{DISL}	dislocation creep grain-size exponent	0	
A_{DISL}	dislocation creep prefactor	1.1×10^5	MPa$^{-3.5}$ s^{-1}
E_{DISL}	dislocation creep activation energy	5.3×10^5	J mol^{-1}
V_{DISL}	dislocation creep activation volume	1.5×10^{-5}	m^3 mol^{-1}
n_{DIFF}	diffusion creep stress exponent	1	
m_{DIFF}	diffusion creep grain-size exponent	3	
A_{DIFF}	diffusion creep prefactor	$10^{7.6}$	μm^{-3} MPa^{-1} s^{-1}
E_{DIFF}	diffusion creep activation energy	3.75×10^5	J mol^{-1}
V_{DIFF}	diffusion creep activation volume	1×10^{-5}	m^3 mol^{-1}